Experimental investigation and simulation of SEM image intensity behaviors for developing thickness-controlled S/TEM lamella preparation via FIB-SEM

Jun Uzuhashi[1,2*], Yuanzhao Yao[2], Tadakatsu Ohkubo[1], and Takashi Sekiguchi[1,2]
[1] *National Institute for Materials Science, Tsukuba, 305-0047, Japan*
[2] *University of Tsukuba, Tsukuba 305-8577, Japan*
[*]Corresponding author. E-mail: UZUHASHI.Jun@nims.go.jp

Keywords: SEM; scanning electron microscopy, FIB; focused ion beam; TEM, transmission electron microscopy

Abstract

High-quality thin lamellae are essential for state-of-the-art scanning transmission electron microscopy (S/TEM) analyses. While the preparation of S/TEM lamellae using focused ion beam (FIB-) scanning electron microscopy (SEM) has been established since the early 21st century, two critical factors have only recently been addressed: precise control over lamella thickness and a systematic understanding of FIB-induced damage. This study conducts an experimental investigation and simulation to explore how the intensities of backscattered and secondary electrons (BSEs and SEs, respectively) depend on lamellae thickness for semiconductor (Si), insulator (Al_2O_3), and metallic (stainless-steel) materials. The BSE intensity shows a simple linear relationship with the lamella thickness for all materials below a certain thickness, whereas the relationship between the SE intensity and thickness is more complex. In conclusion, the BSE intensity is a reliable indicator for accurately determining lamella thickness across various materials during FIB thinning processing, while the SE intensity lacks consistency due to material and detector variability. This insight enables the integration of real-time thickness control into S/TEM lamella preparation, significantly enhancing lamella quality and reproducibility. These findings pave the way for more efficient, automated processes in high-quality S/TEM analysis, making the preparation method more reliable for a range of applications.

Introduction

Transmission electron microscopy (TEM) and scanning TEM (STEM) are essential tools for atomic-scale microstructure analysis [1,2]. Aberration correction technology has greatly enhanced the effectiveness of these analytical techniques [3–6]. Alongside advancements in the S/TEM technique, the development of the S/TEM lamellae preparation method using a focused Ga ion beam (FIB) with scanning electron microscopy (SEM) has enabled high-throughput, site-specific lamellae preparation [7–10]. State-of-the-art S/TEM instruments demand high-quality lamellae. However, it is well known that the Ga^+ beam induces damage to target materials [9–18]. Therefore, producing high-quality S/TEM lamellae requires achieving sufficient thinness while minimizing FIB-induced damage. Conventionally, FIB-SEM operators determine the endpoint of thinning based on their own experience and skill [19–21]. Recently, automated FIB fabrication methods have been developed to provide reproducibility, high throughput, and statistical reliability [19,21–25]. However, current automation methods for S/TEM lamellae rely on pre-defined FIB milling recipes without incorporating thickness measurement. Several approaches have been explored to integrate quantitative lamellae thickness measurement into the FIB-SEM process [19,20,24,26–28]. However, ideally, thickness measurement should be performed simultaneously with the lamellae-thinning FIB process. This study revealed the relationship between SEM intensity behaviors and lamellae thickness, demonstrating that combining precise thickness control with an understanding of FIB-induced damage enables a solid strategy for producing high-quality TEM lamellae.

Methods

A Helios 5UX FIB-SEM dual-beam system equipped with AutoScript (Thermo Fisher Scientific) was used. Conventional Everhart–Thornley and through-the-lens detectors (ETD and TLD, respectively) were used for SEM imaging. The retractable backscattered electron (BSE) and STEM detectors were excluded as candidates due to their impossibility with concurrent use during the FIB thinning process. The dependence of secondary electron (SE) and BSE intensities on different acceleration voltages was investigated using wedge-shaped chunks of Si, Al_2O_3 (single crystal sapphire), and SUS304 stainless steel (Fe_{bal}-$Cr_{18\sim20}$-$Ni_{8\sim10.5}$), as these materials represent typical semiconductors, insulators, and metallic materials, respectively. **Fig. 1a** shows the top-view SEM image of the wedge-shaped chunk. The chunk was observed cross-sectionally, confirming that its thickness increased linearly. Wedge-shaped chunks of Si, Al_2O_3, and stainless steel were prepared by FIB milling at 8 kV. **Fig. 1b** shows the positional relationship for SEM imaging of the chunk in this study, with α representing the coincidence angle of the SEM and FIB beams, 52° in the Helios 5UX system. **Fig. 1c** shows the inside of the vacuum chamber of the FIB-SEM system, along with a schematic of the positional information of the detectors (ETD and TLD). All SEM images were obtained with a beam current of 800 pA and a dwell time of 3 µs. Since this work aims to measure lamellae thickness during the FIB thinning, the reason for choosing these values is as follows. In general, a lower beam current or a shorter dwell time makes the SEM image quality poor since the number of emitted electrons decreases, and a higher beam current degrades spatial resolution due to its larger beam spot size [29,30]. If a longer dwell time is adopted; it may cause the specimen to drift during the FIB thinning process. Electrons with energies below 50 eV were classified as SEs, while those with energies above 50 eV were referred to as BSEs [29,30]. The incident of the primary electron beam with the sample produced various signals, including both SEs and BSEs. The interaction volume of induced electrons was called the "electron range". SEs escaped from surface regions within a few to tens of nanometers, while BSEs were emitted from deeper within the material, typically ranging from several hundred nanometers to a few micrometers [29,30]. The ETD is classified as an “out-lens” or “in-chamber” type detectors due to its positioning, and it is commonly used for collecting SEs. In contrast, the TLD was located within the SEM column (**Fig. 1c and 2**), making it an “in-lens” type detector that collects both SEs and BSEs. In the Helios 5UX system, the TLD could be operated with or without a magnetic immersion lens, as shown in **Fig. 2**. When in the magnetic immersion lens mode, the sample was immersed in the magnetic lens, allowing the TLD to collect electrons emitted from both the upper and lower surfaces of the sample, which is a capability that differs from the field-free mode. A Java Monte Carlo simulation for SEs (JMONSEL) was used to analyze these three materials at different accelerating voltages to interpret the underlying mechanisms of lamellae thickness measurement using SEM imaging [31]. This simulator was based on Monte Carlo modeling of inelastic or elastic scattering processes occurring in the bulk as a result of the interaction between the incident electron beam and material [32]. Detailed information on the functionality of the JMONSEL simulator is presented in previous studies [33,34].

Results and Discussion

Fig. 3 shows SEM images of a wedged-shaped Si chunk at different accelerating voltages, including SE images obtained by the ETD (ETD-SE), SE images from the TLD without a magnetic immersion lens (TLD-SE (Field-Free)), and BSE images by the TLD (TLD-BSE). The Si thickness increased linearly from 0 to 500 nm, moving from the bottom to the top, with the top surface protected by Pt deposition. It should be noted that the formation of 8 kV FIB-damaged amorphized layers would affect the SEM images of extremely thinner regions below 20 nm [9,11,15,18]. SE images from the TLD with and without the magnetic immersion lens (“TLD-SE (Immersion)”) are shown in **Supplementary Fig. 1**, exhibiting trends similar to those of the ETD-SE images. Notably, the SE intensity was enhanced in the thinner region, especially in the ETD-SE images at an accelerating

voltage of 5 kV. In contrast, the thinner areas appeared darker in the TLD-SE (Field-Free) and TLD-BSE (Immersion) images. All SE/BSE images obtained for Al_2O_3 and stainless steel at accelerating voltages from 5 to 30 kV are presented in **Supplementary Fig. 2 and 3**, respectively. The "TLD-BSE (Field-Free)" images exhibited the same trend as the TLD-BSE (Immersion) images but with significantly lower quality due to reduced BSE collection by the detector (**Supplementary Fig. 4**).

Fig. 4 shows the normalized SE and BSE intensity profiles for Si, Al_2O_3, and stainless steel as a function of chunk thickness at different accelerating voltages. The intensities' line profiles were drawn by integrating 100-pixel-width as shown in **Fig. 3** using the pixel intensities (8.993 nm/pixel in this study). Then, these profiles were normalized based on the maximum value in the thick bulk region (~2 μm) and the minimum in the vacuum region. Note that the regions showing the edge effect were excluded in the case of SE images. In the Si and stainless-steel cases, the intensities of ETD-SE (**Fig. 4a and 4c**) increased sharply at the vacuum–sample interface, followed by a gradual increase and eventual decrease. The thickness at which the lamellae showed the brightest contrast increased with the acceleration voltage. TLD-SE (Field-Free) (**Fig. 4d and 4f**) also showed a sharp increase in intensity from the vacuum to the sample, continuing to rise but saturating at certain thicknesses. The SE intensities for Al_2O_3 are different from those of Si and stainless steel, likely due to its insulating properties (**Fig. 4b and 4e**). In contrast, all BSE intensities increased linearly with thickness, also saturating at a certain point (**Fig. 4g–i**). This trend aligned with findings from previous studies on metal coatings [28–30,35–38] and thin lamellae in a vacuum using BSE intensity [24,27]. The SE and BSE intensity trends for Si and stainless steel were similar in ETD-SE, TLD-SE, and TLD-BSE, with the only difference being the thicknesses corresponding to maximum intensity in ETD-SE and saturation thicknesses in TLD-SE (Field-Free) and TLD-BSE. Notably, the saturation thicknesses for TLD-SE (Field-Free) and TLD-BSE were the same for both Si (**Fig. 4d and 4g**) and stainless steel (**Fig. 4f and 4i**).

The JMONSEL simulation was applied on wedge-shaped chunks arranged according to the positional relationship depicted in **Fig. 1b** and **5a** to elucidate the characteristic behaviors of SEs and BSEs. In **Fig. 5a**, the primary electron beam is illustrated with yellow lines, while blue circles indicate the electron range. Red lines indicate SEs emitted from the surface of the lamellae. The simulation was used to calculate the total, upwards, and downwards SE yields, as well as the upwards and downwards BSE yields as functions of chunk thickness, which are presented in **Fig. 5b and 5c**. The total SE, referred to as "SE_{total}", yield exhibited a gradual increase followed by a decrease in the thicker region. In contrast, the upwards SE ("$SE_{upwards}$") yield increased with thickness and reached saturation at a certain thickness. The simulated SE_{total} yield was quite similar to the experimental trend of ETD-SE (**Fig. 4a**), while the $SE_{upwards}$ yield resembled the TLD-SE (Field-Free) trend (**Fig. 4d**). The experimental results for TLD-BSE aligned well with the simulated upwards BSE ("$BSE_{upwards}$") yield (**Fig. 4g**). In contrast, the downwards BSE ("$BSE_{downwards}$") yield consistently decreased with increasing thickness, as the possibility of electron transmission approached 0 in the thicker region.

Fig. 6 summarizes the simulated results for SE_{total}, $SE_{upwards}$, and $BSE_{upwards}$ yields. The electron ranges were simulated by considering the material densities (2,330 kg/m^3 for Si, 4,000 kg/m^3 for Al_2O_3, and 7,874 kg/m^3 for Fe). Consequently, the sizes of the electron ranges followed the order: $Si > Al_2O_3 > Fe$ (**Supplementary Fig. 5**). With increasing acceleration voltage, the electron range also expanded. Both the simulated $BSE_{upwards}$ yield (**Fig. 6g–i**) and experimental TLD-BSE intensity (**Fig. 4g–i**) increased with good linearity, reaching saturation at a certain thickness. The BSE yield was influenced by the part of the electron interaction volume within the lamellae, which is shown as the blue region in **Fig. 5a**. Therefore, it could be concluded that the $BSE_{upwards}$ yield had a linear relationship with the lamellae thickness, transitioning to saturation once the lamellae thickness exceeded the electron interaction volume. In both experimental (**Fig. 4**) and simulation results (**Fig. 6**), the saturation thicknesses followed the same order: $Si > Al_2O_3 > Fe$, corresponding to the electron

range order (**Supplementary Fig. 6**). The electron range increased with the accelerating voltage, leading to a corresponding increase in saturation thickness.

The $BSE_{upwards}$ was mainly detected by the TLD because the detector was positioned above the sample, allowing BSEs, which have higher energies and travel in straight paths, to be collected efficiently. This simple and linear behavior of the $BSE_{upwards}$ intensity facilitated the lamellae thickness measurement. In the case of SEs, the experimental ETD-SE (**Fig. 4a and 4c**) and simulated SE_{total} yield (**Fig. 6a and 6c**) exhibited similar trends, indicating that ETD mainly collected SE_{total}. Tian *et al.* [27] explained that the SE_{total} intensity could be considered as the sum of three components: (1) SEs generated by the primary electron beam, (2) SEs generated within the electron range, and (3) downwards-emitted SEs ($SE_{downwards}$). While SE generation from the primary electron beam remained constant, SEs generated by the electron range increased until saturation, while the $SE_{downwards}$ decreased 0. The sum of these three factors resulted in the SE_{total} intensity. Therefore, the saturation thicknesses for the $SE_{upwards}$ yield (**Fig. 6d–f**) aligned with the maximum SE_{total} yield thicknesses (**Fig. 6a–c**) and the saturation points for $BSE_{upwards}$ (**Fig. 6g–i**).

Compared with experimental results, it appeared that ETD-SE mainly collected SE_{total}, while TLD-SE (Field-Free) captured $SE_{upwards}$. It should be emphasized that the SE intensity did not reach its maximum in the thinnest region, regardless of the detector used. However, deviations were observed between the experimental and simulated results. Specifically, the simulated thicknesses corresponding to the maximum intensity in ETD-SE and saturated points for TLD-BSE and TLD-SE (Field-Free) were 1.5 to 3 times larger than the experimental results. To compare the simulated predictions with the experimental results, it was crucial to consider the acceptances of SEs and BSEs by the detectors.

The trajectories of BSEs were nearly straight due to their high energies, which meant that the acceptance of BSE detectors was proportional to the number of released BSEs. Consequently, our simulation results were in good agreement with the features in the experimental data. In contrast, SE trajectories were easily influenced by electric fields, making the estimation of SE acceptance difficult. As a result, the deviations between the experimental and simulated SE results were larger than those of the BSEs.

Currently, experimental results serve as the most reliable reference for assessing the S/TEM lamellae thicknesses. This reliability is due to the ongoing advancements by FIB-SEM companies in detector technology, resulting in complexities regarding SE and BSE acceptances. This study confirmed that lamellae thickness measurement using TLD-BSE ($BSE_{upwards}$) is suitable for a wide range of materials by using their linearity with the appropriate accelerating SEM voltage.

Concluding Remarks

In summary, our experimental and simulation investigation demonstrated that only the intensity of the $BSE_{upwards}$ could be reliably used to determine lamellae thickness for a wide range of materials, including insulators. However, the behavior of SE intensity was strongly affected by material properties or detector selection, making it difficult to use for quantitative thickness control. Conventionally, S/TEM lamellae preparation recipes were defined solely by FIB parameters. However, the ability to measure lamellae thickness simultaneously and accurately allowed us to incorporate thickness parameters into the thinning recipe, leading to higher-quality and reliable S/TEM analyses.

References

1. Williams D.B., Carter C.B., (1996) *Transmission Electron Microscopy - A Textbook for Materials Science*, Springer New York, New York. https://doi.org/10.1007/978-1-4757-2519-3
2. Kohl H., Reimer L., (2008) *Transmission Electron Microscopy - Physics of Image Formation and Microanalysis*, Springer New York, New York. https://doi.org/10.1007/978-0-387-40093-8
3. Haider M., Rose H., Uhlemann S., Schwan E., Kabius B., Urban K., (1998) *A spherical-aberration-corrected 200 kV transmission electron microscope*, Ultramicroscopy **75**, 53–60.

https://doi.org/10.1016/S0304-3991(98)00048-5
4. Krivanek O.L., Dellby N., Lupini A.R., (1999) *Towards sub-Å electron beams*, Ultramicroscopy **78**, 1–11. https://doi.org/10.1016/S0304-3991(99)00013-3
5. Krivanek O.L., Nellist P.D., Dellby N., Murfitt M.F., Szilagyi Z., (2003) *Towards sub-0.5 Å electron beams*, Ultramicroscopy **96**, 229–237. https://doi.org/10.1016/S0304-3991(03)00090-1
6. Urban K.W., (2008) *Studying atomic structures by aberration-corrected transmission electron microscopy*, Science **321**, 506–510. https://doi.org/10.1126/science.1152800
7. Giannuzzi L.A., Stevie F.A., (1999) *A review of focused ion beam milling techniques for TEM specimen preparation*, Micron **30**, 197–204. https://doi.org/10.1016/S0968-4328(99)00005-0
8. Volkert C.A., Minor A.M., (2007) *Focused ion beam microscopy and micromachining*, MRS Bulletin **32**, 389–399. https://doi.org/10.1557/mrs2007.62
9. Kato N.I., Kohno Y., Saka H., (1999) *Side-wall damage in a transmission electron microscopy specimen of crystalline Si prepared by focused ion beam etching*, Journal of Vacuum Science and Technology A **17**, 1201. https://doi.org/10.1116/1.581795
10. Kato N.I., (2004) *Reducing focused ion beam damage to transmission electron microscopy samples*, Journal of Electron Microscopy **53**, 451–458. https://doi.org/10.1093/jmicro/dfh080
11. Giannuzzi L.A., Geurts R., Ringnalda J., (2005) *2 keV Ga^+ FIB milling for reducing amorphous damage in silicon*, Microscopy and Microanalysis **11**, 828–829. https://doi.org/10.1017/S1431927605507797
12. Lotnyk A., Poppitz D., Ross U., Gerlach J.W., Frost F., Bernütz S., Thelander E., Rauschenbach B., (2005) *Focused high- and low-energy ion milling for TEM specimen preparation*, Microelectronics Reliability **55**, 2119–2125. https://doi.org/10.1016/j.microrel.2015.07.005
13. Thompson K., Gorman B., Larson D.J., Leer B.V., Hong L., (2006) *Minimization of Ga induced FIB damage using low energy clean-up*, Microscopy and Microanalysis **12**, 1736–1737. https://doi.org/10.1017/S1431927606065457
14. Giannuzzi L.A., (2006) *Reducing FIB damage using low energy ions*, Microscopy and Microanalysis **12**, 1260–1261. https://doi.org/10.1017/S1431927606065469
15. Mayer J., Giannuzzi L.A., Kamino T., Michael J., (2007) *TEM sample preparation and FIB-induced damage*, MRS Bulletin **32**, 400–407. https://doi.org/10.1557/mrs2007.63
16. Schaffer M., Schaffer B., Ramasse Q., (2012) *Sample preparation for atomic-resolution STEM at low voltages by FIB*, Ultramicroscopy **114**, 62–71. https://doi.org/10.1016/j.ultramic.2012.01.005
17. Sato T., Nakano K., Matsumoto H., Torikawa S., Nakatani I., Kiyohara M., Isshiki T., (2017) *High quality lamella preparation of gallium nitride compound semiconductor using Triple Beam system*, Journal of Physics: Conference Series **902**, 012019. https://doi.org/10.1088/1742-6596/902/1/012019
18. Uzuhashi J., Ohkubo T., (2024) *Systematic study of FIB-induced damage for the high-quality TEM sample preparation*, Ultramicroscopy **262**, 113980. https://doi.org/10.1016/j.ultramic.2024.113980
19. Volkenandt T., Pérez-Willard F., Rauscher M., Anger P.M., (2017) *Towards automatic lamella thinning using live thickness measurements and smart end-point detection*, Microscopy and Microanalysis **23**, 304–305. https://doi.org/10.1017/S1431927617002203
20. Conlan A.P., Tillotson E., Rakowski A., Cooper D., Haigh S.J., (2020) *Direct measurement of TEM lamella thickness in FIB-SEM*, Journal of Microscopy **279**, 168–176. https://doi.org/10.1111/jmi.12852
21. Tsurusawa H., Nakanishi N., Kawano K., Chen Y., Dutka M., Leer B.V., Mizoguchi T., (2021) *Robotic fabrication of high-quality lamellae for aberration-corrected transmission electron microscopy*, Scientific Reports **11**, 21599. https://doi.org/10.1038/s41598-021-00595-x
22. Leer B.V., Geurts R., Scharfschwerdt R., Cheng H., Li L., Imlau R., (2018) *New workflows broaden access to S/TEM analysis and increase productivity*, Microscopy Today **26**, 18–25.

https://doi.org/10.1017/S1551929517001195
23. Uzuhashi J., Ohkubo T. and Hono K., (2023) *Development of automated tip preparation for atom probe tomography by using script-controlled FIB-SEM*, Ultramicroscopy **247**, 113704. https://doi.org/10.1016/j.ultramic.2023.113704
24. Tsurusawa H., Uzuhashi J., Kozuka Y., Kimoto K., Ohkubo T., (2024) *Robust preparation of sub-20-nm-thin lamellae for aberration-corrected transmission electron microscopy*, Small Methods **8**, 2301425. https://doi.org/10.1002/smtd.202301425
25. Uzuhashi J., Ohkubo T. and Hono K., (2024) *An automated site-specific tip preparation method for atom probe tomography using script-controlled focused ion beam/scanning electron microscopy*, Microscopy and Microanalysis **30**, ozae015. https://doi.org/10.1093/mam/ozae015
26. Salzer R., Graff A., Simon M., Altmann F., (2009) *Standard free thickness determination of thin TEM samples via backscatter electron image correlation*, Microscopy and Microanalysis **15**, 340 –341. https://doi.org/10.1017/S1431927609096457
27. Tian J., Wu J., Chiu Y-L., (2018) *Monte Carlo simulation and theoretical calculation of SEM image intensity and its application in thickness measurement*, Ultramicroscopy **187**, 12–19. https://doi.org/10.1016/j.ultramic.2018.01.004
28. Skoupy R., Fort T., Krzyzanek V., (2020) *Nanoscale estimation of coating thickness on substrates via standardless BSE detector calibration*, Nanomaterials **10**, 332. https://doi.org/10.3390/nano10020332
29. Reimer L., (1998) *Scanning Electron Microscopy -Physics of Image Formation and Microanalysis*, Springer Berlin, Heidelberg. https://doi.org/10.1007/978-3-540-38967-5
30. Ul-Hamid A., (2019) *A Beginners' Guide to Scanning Electron Microscopy*, Springer Cham, Zurich. https://doi.org/10.1007/978-3-319-98482-7
31. Ritchie N.W.M., (2005) *A new Monte Carlo application for complex sample geometries*, Surface and Interface Analysis **37**, 1006–1011. https://doi.org/10.1002/sia.2093
32. Joy D.C., (1995) *Monte Carlo modeling for electron microscopy and microanalysis*, Oxford University Press, New York. https://doi.org/10.1093/oso/9780195088748.001.0001
33. Villarrubia J.S., Vladár A.E., Postek M.T., (2005) *Scanning electron microscope dimensional metrology using a model-based library*, Surface and Interface Analysis **37**, 951–958, https://doi.org/10.1002/sia.2087
34. Villarrubia J.S., Vladár A.E., Ming B., Kline R.J., Sunday D.F., Chawla J.S., List S., (2015) *Scanning electron microscope measurement of width and shape of 10 nm patterned lines using a JMONSEL-modeled library*, Ultramicroscopy 154, 15–28. https://doi.org/10.1016/j.ultramic.2015.01.004
35. Kanaya K., Okayama S., (1972) *Penetration and energy-loss theory of electrons in solid targets*, Journal of Physics D: Applied Physics **5**, 43. https://doi.org/10.1088/0022-3727/5/1/308
36. Niedrig H., (1977) *Film-thickness determination in electron microscopy: The electron backscattering method*, Journal of Modern Optics **24**, 679–691. http://dx.doi.org/10.1080/713819609
37. Niedrig H., (1982) *Electron backscattering from thin film*, Journal of Applied Physics **53**, 15–24. http://dx.doi.org/10.1063/1.331005
38. Rajora O.S., Curzon A.E., (1985) *A simple method for the determination of film thickness from electron image contrast in a scanning electron microscope*, Thin Solid Films **123**, 235–238. https://doi.org/10.1016/0040-6090(85)90163-4

Figure 1

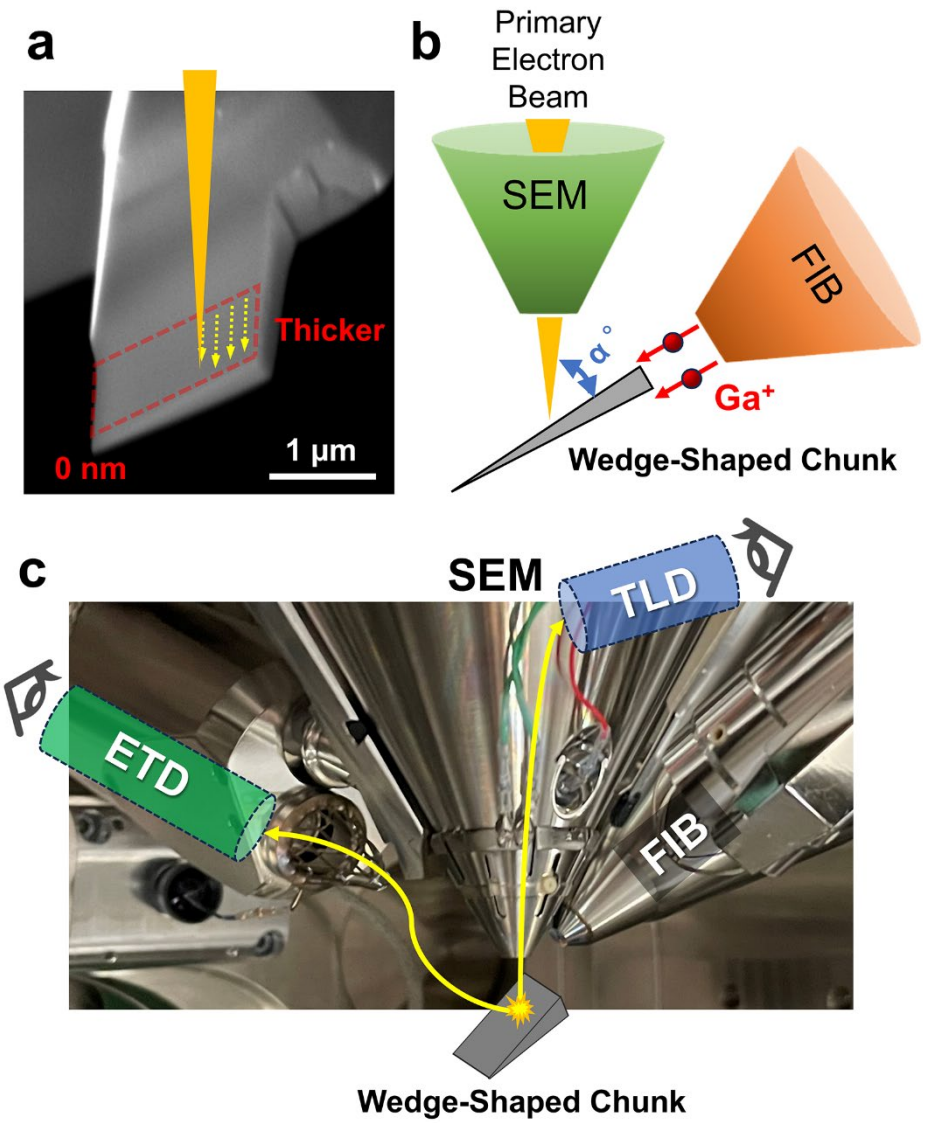

Figure 1. (a) Top-view scanning electron microscopy (SEM) image of the wedge-shaped chunk with a schematic illustrating primary electron scanning. (b) Schematic of the positional relationship for SEM imaging of the wedge-shaped chunk, which is consistent with the relationship used in scanning transmission electron microscopy (S/TEM) lamella preparation. (c) The vacuum chamber of the focused ion beam (FIB)-SEM system showing the positional information of the Everhart–Thornley and through-the-lens detectors (ETD and TLD, respectively).

Figure 2

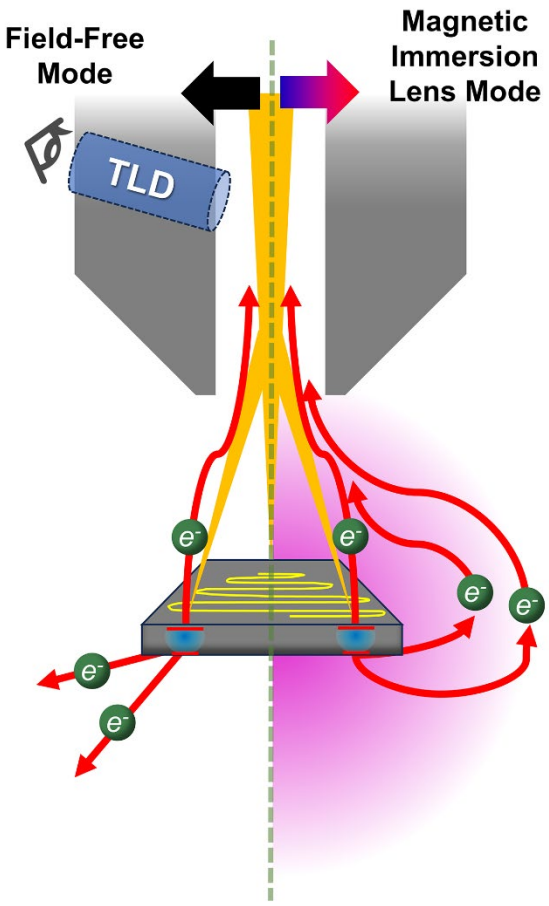

Figure 2. Schematic illustrating the "Field-Free" and "Magnetic Immersion Lens" modes of the TLD.

Figure 3

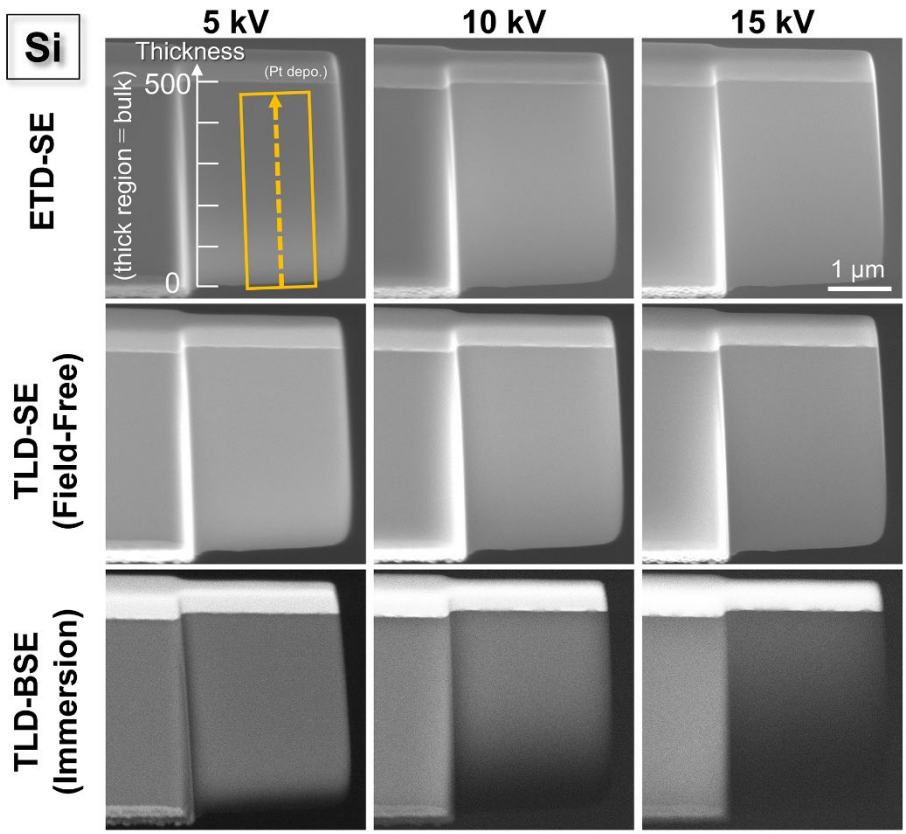

Figure 3. Secondary electron (SE) images captured by the ETD ("ETD-SE"), SE images from the TLD without the magnetic immersion lens ("TLD-SE (Field-Free)"), and backscattered electron (BSE) images from the TLD ("TLD-BSE") at accelerating voltages of 5, 10, and 15 kV.

Figure 4

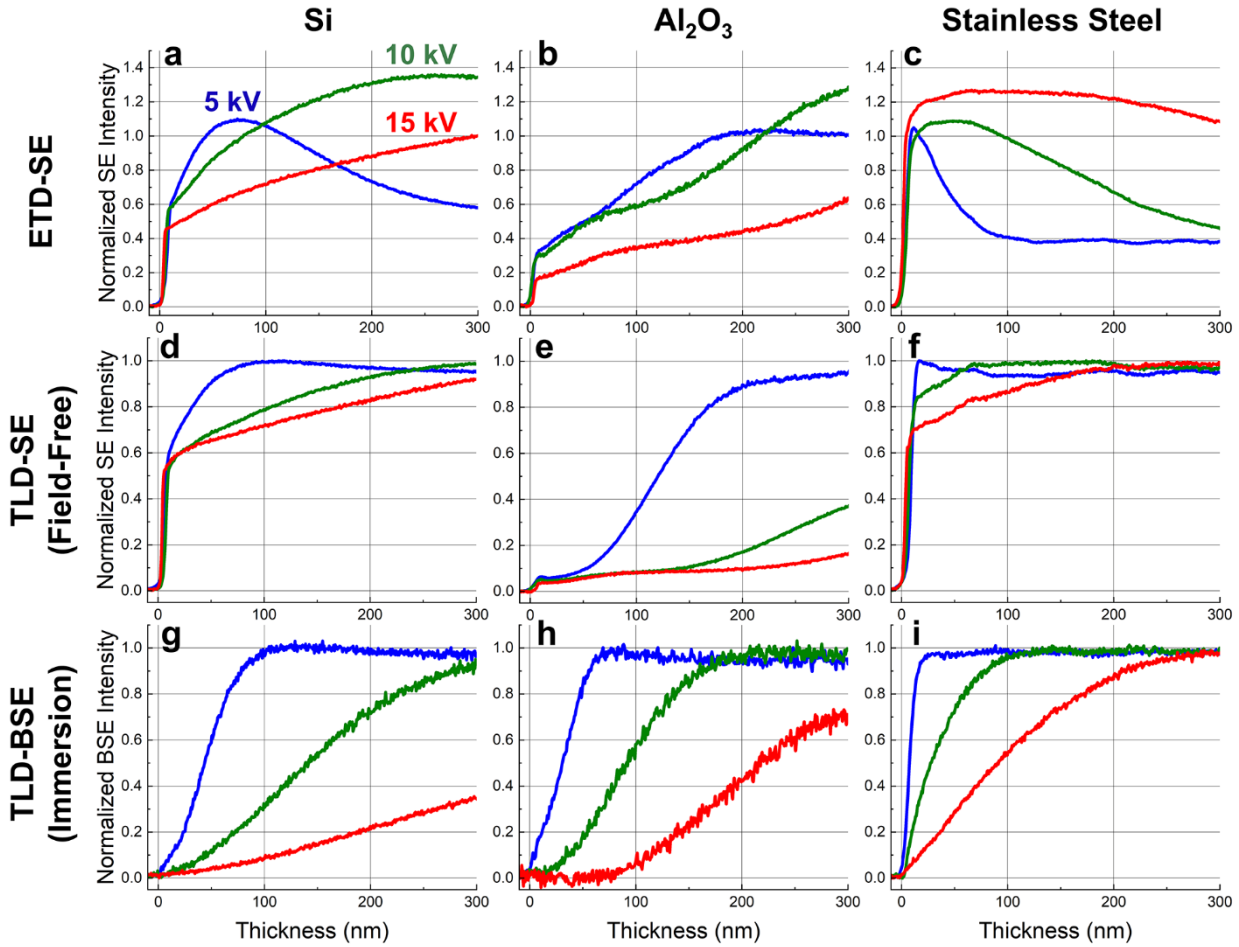

Figure 4. Normalized SE and BSE intensity profiles for Si, Al_2O_3, and stainless-steel chunks as a function of thickness (0–300 nm) at varying accelerating voltages (5, 10, and 15 kV).

Figure 5

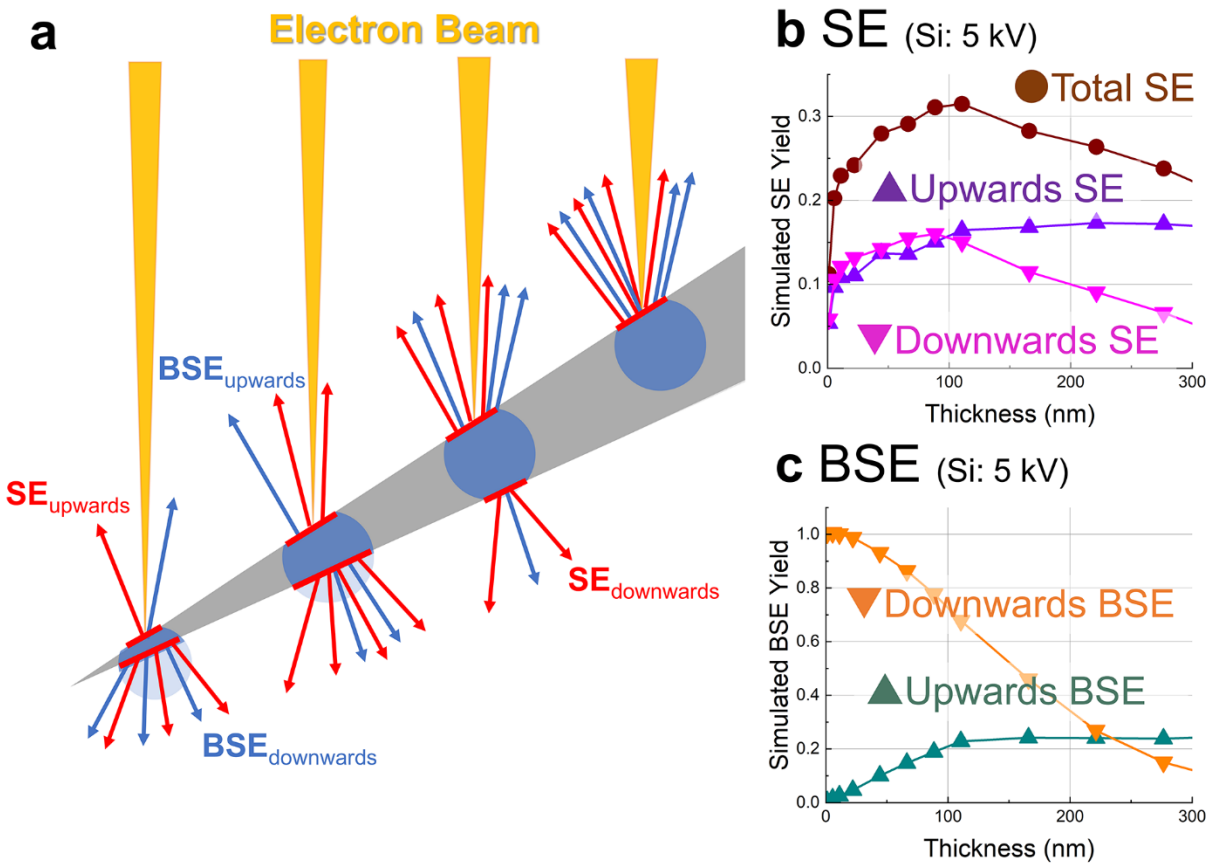

Figure 5. (a) Schematic illustrating SE and BSE emission from a wedge-shaped specimen. (b) Simulated total and upwards SE yields, and (c) upwards and bottomwards BSE yields for the Si wedge-shaped specimen at 5 kV.

Figure 6

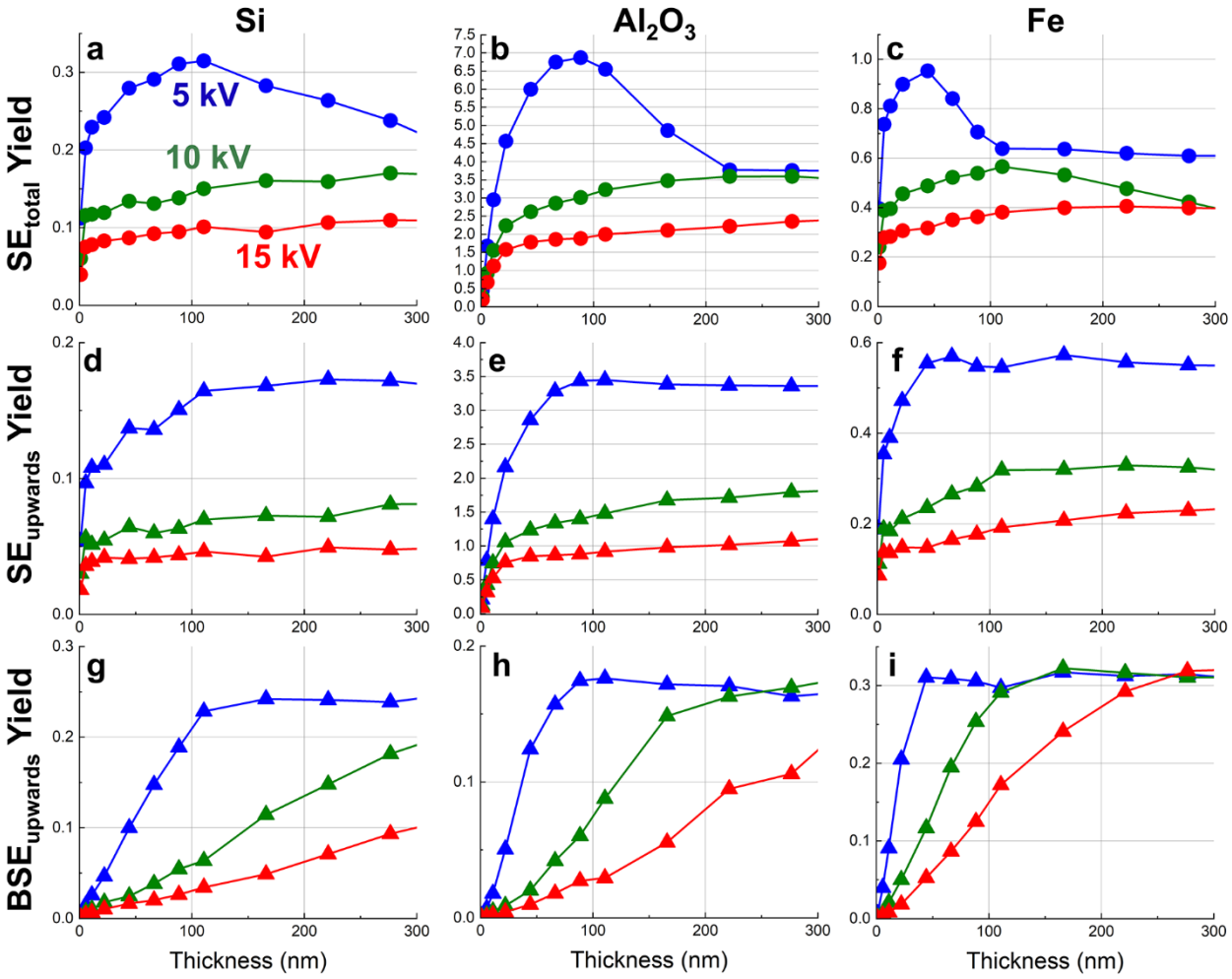

Figure 6. Simulated yields of the SE_{total}, $SE_{upwards}$, and $BSE_{upwards}$ for Si, Al_2O_3, and Fe at accelerating voltages of 5, 10, and 15 kV.

Supplementary Figure 1

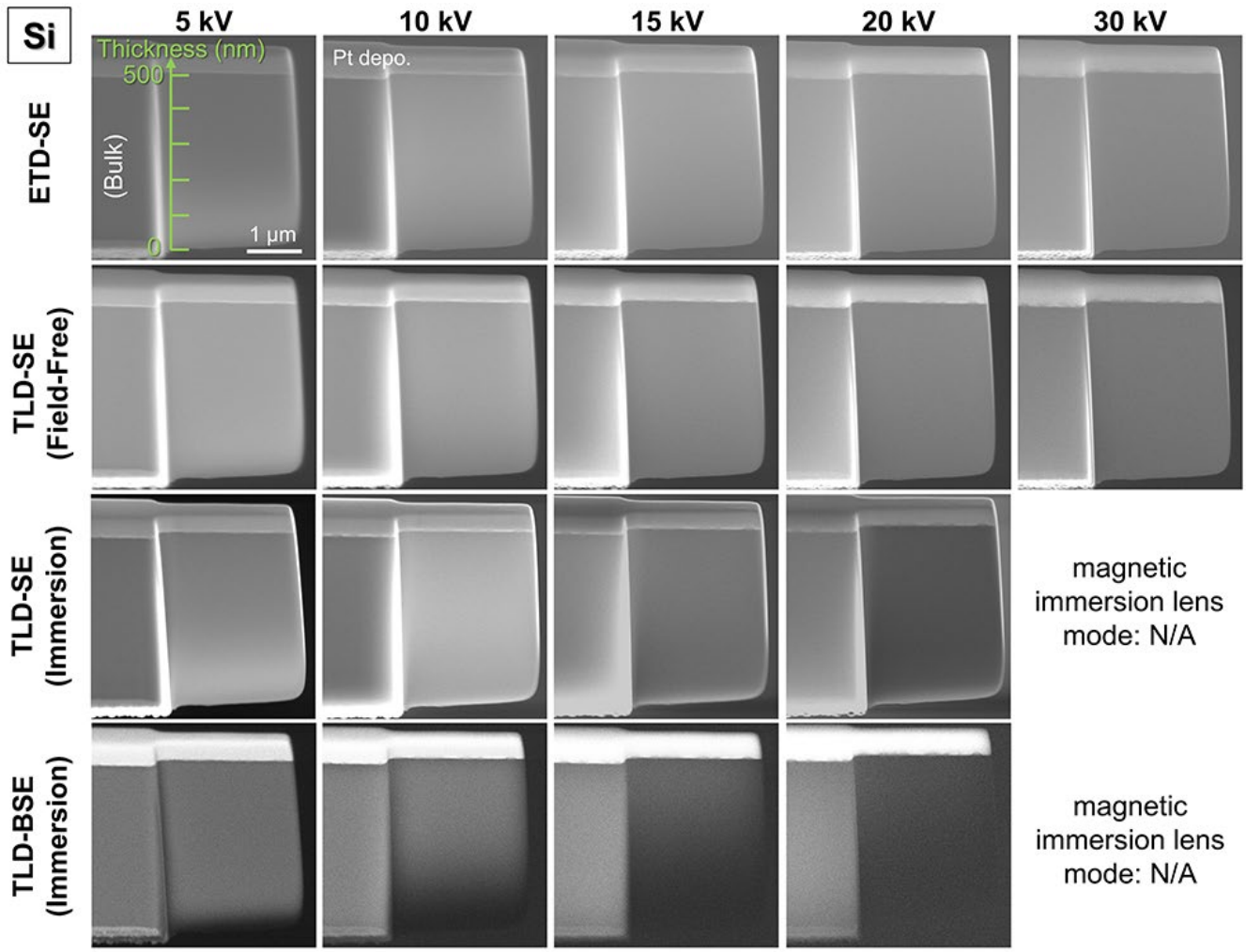

Supplementary Figure 1. Secondary and backscattered electron (SE and BSE, respectively) images of an Si wedge-shaped chunk at accelerating voltages of 5 to 30 kV.

Supplementary Figure 2

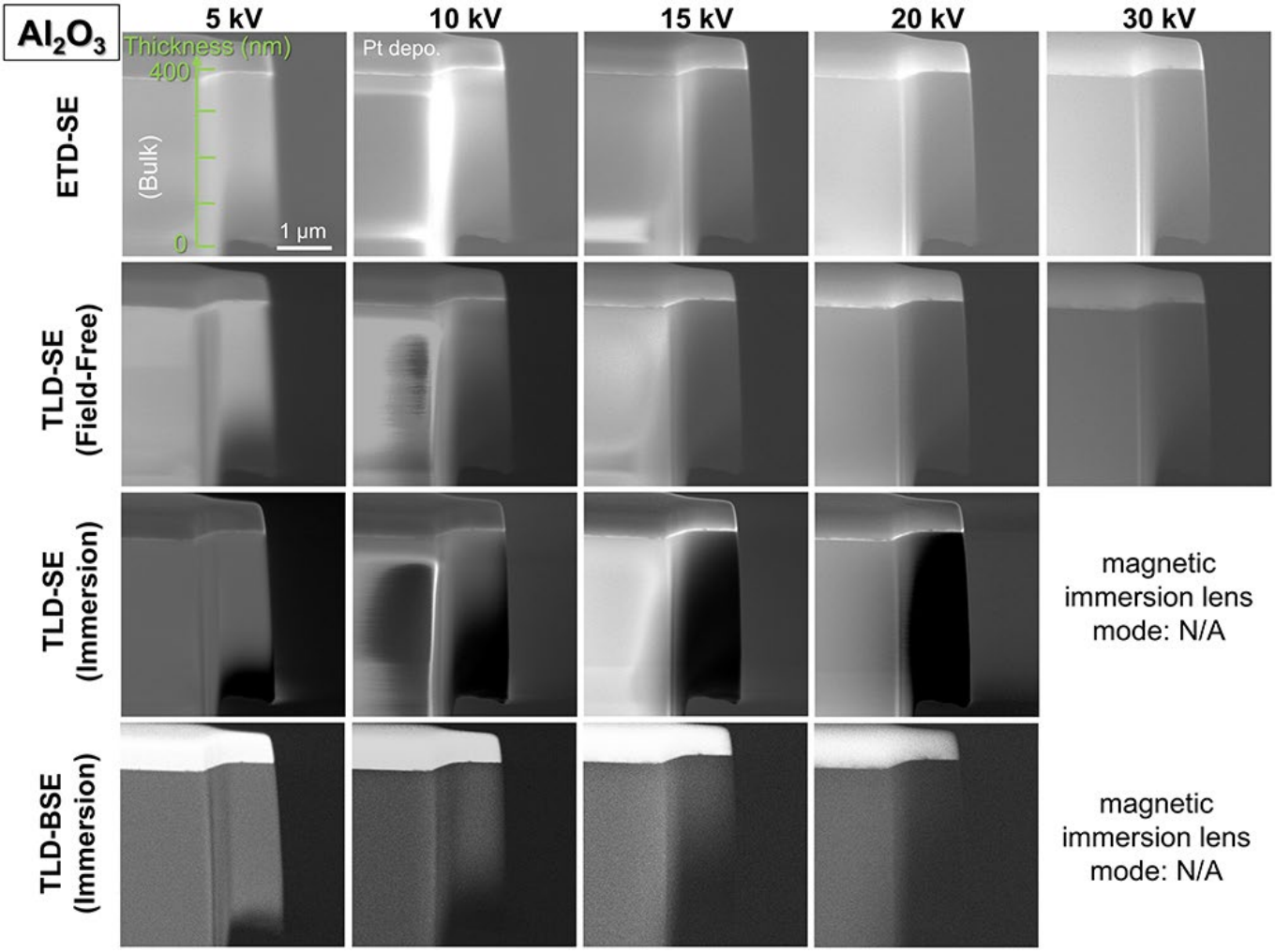

Supplementary Figure 2. SE and BSE images of an Al_2O_3 wedge-shaped chunk at accelerating voltages of 5 to 30 kV.

Supplementary Figure 3

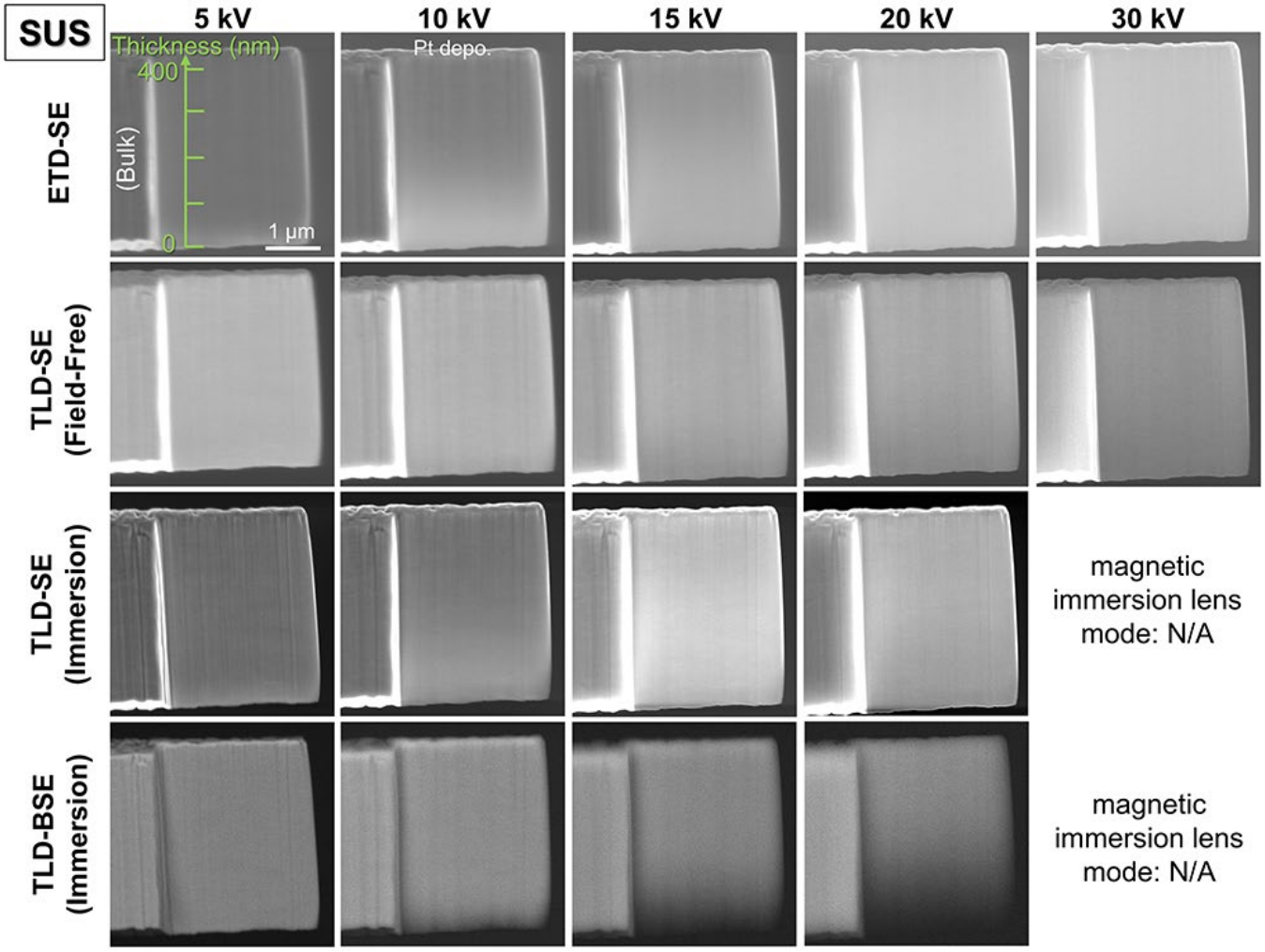

Supplementary Figure 3. SE and BSE images of a stainless-steel wedge-shaped chunk at accelerating voltages of 5 to 30 kV.

Supplementary Figure 4

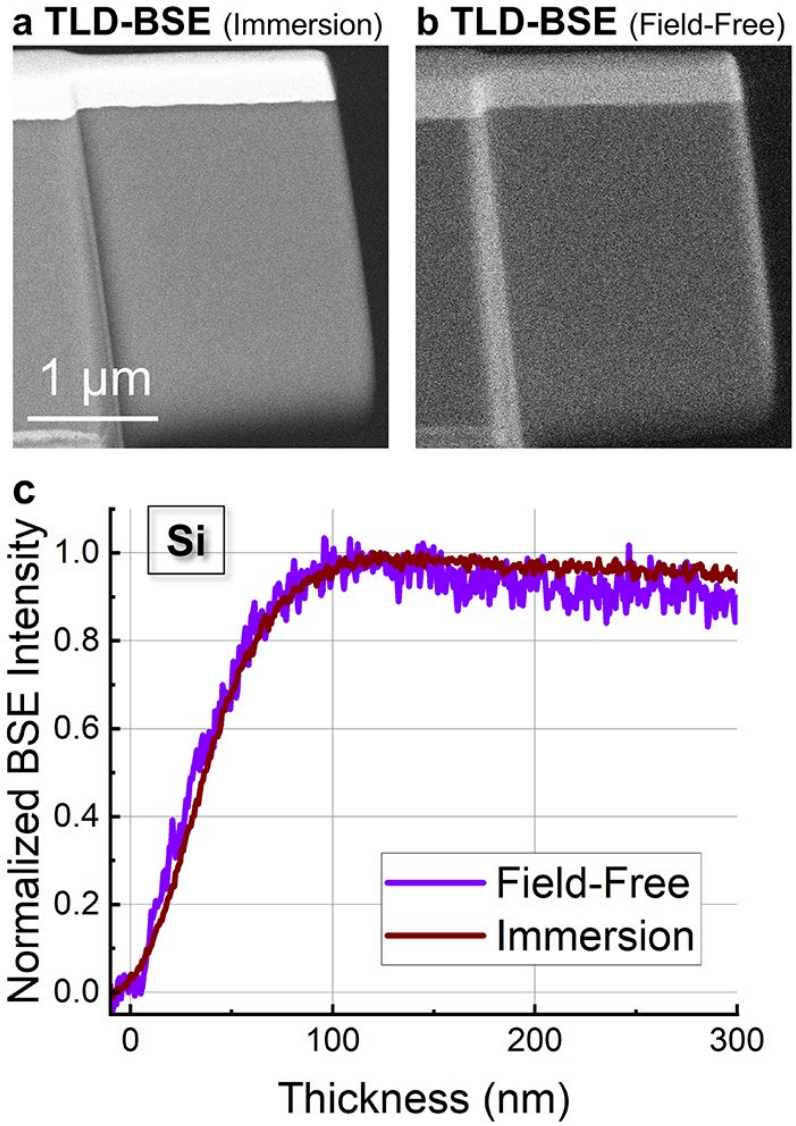

Supplementary Figure 4. (a, b) BSE images of Si wedge-shaped chunk captured by a through-the-lens detector (TLD) (a) with and (b) without a magnetic immersion lens ("TLD-BSE (Immersion)" and "TLD-BSE (Field-Free)") at 5 kV. (c) Normalized BSE intensity profiles as a function of the chunk thickness.

Supplementary Figure 5

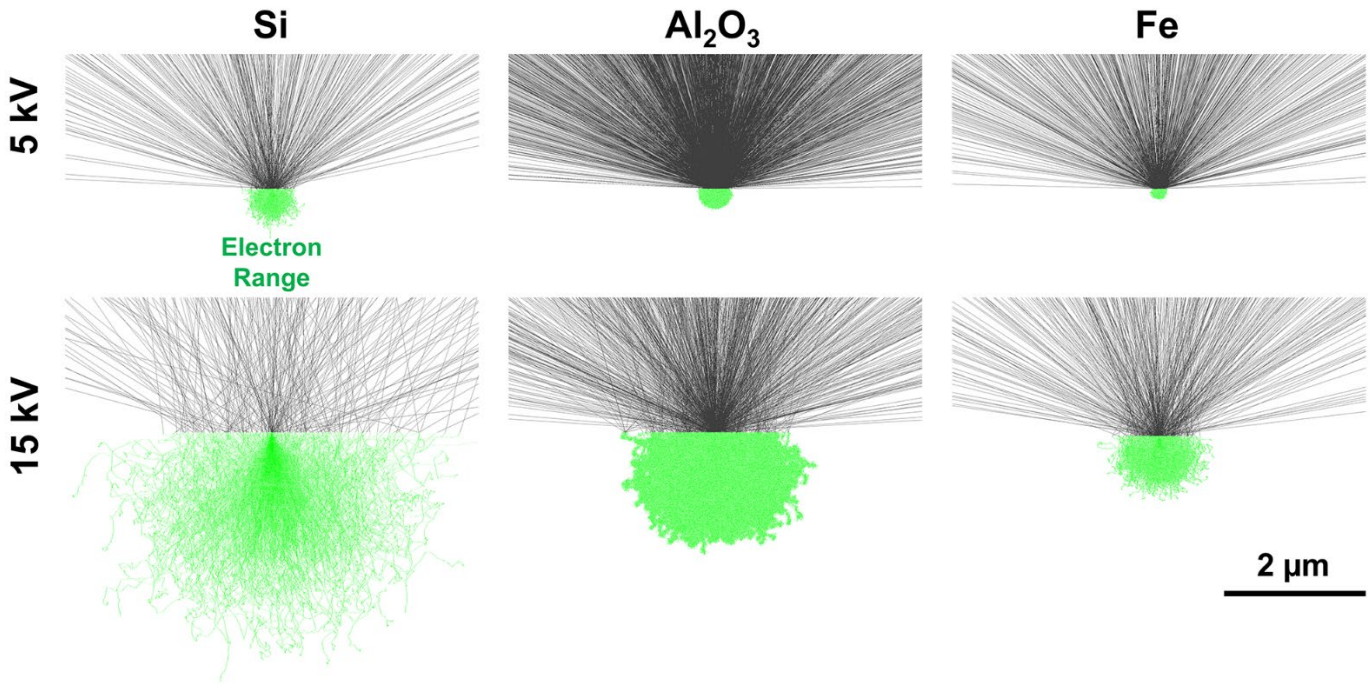

Supplementary Figure 5. Simulation results for the interaction of a primary electron beam with bulk Si, Al_2O_3, and Fe. The green lines indicate the electron ranges, illustrating the tragedies of electron interactions, with interaction volumes ordered as Si > Al_2O_3 > Fe for the same acceleration voltage. The black lines indicate the emitted electrons from the surface. As the acceleration voltage increases, the electron range also expands. The SE escape depths at 5 kV are 40 nm for Si, 75 nm for Al_2O_3, and 6.5 nm for Fe.

Supplementary Figure 6

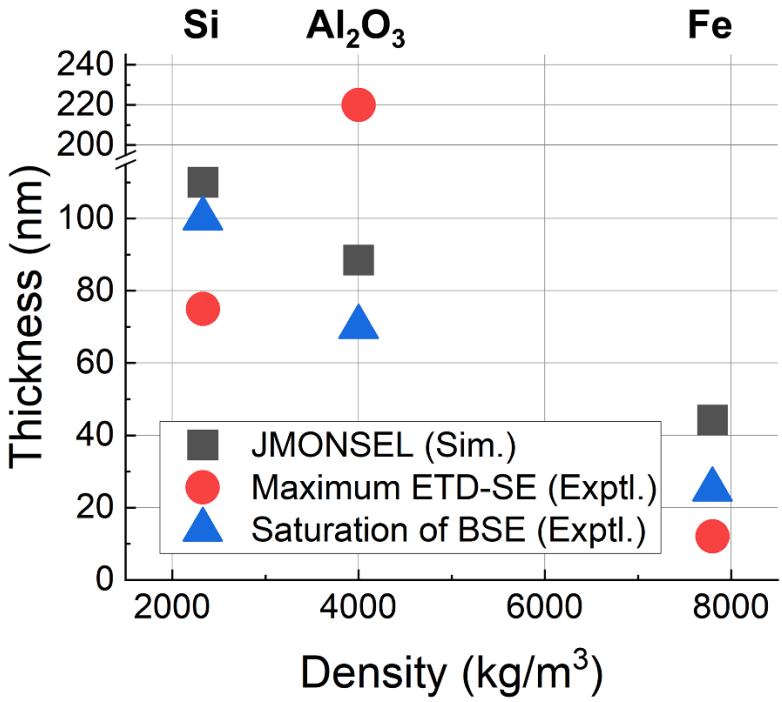

Supplementary Figure 6. Dependence of SEM intensity as a function of the materials' density at 5 kV. JMONSEL simulation results for the thicknesses of maximum SE_{total}, saturation point of $SE_{upwards,}$ and $BSE_{upwards}$ are plotted by black-colored squares. Red-colored circles indicate the experimental thicknesses of ETD-SE intensities become the maximum and blue-colored triangles show the points of TLD-BSE intensities are saturated. The JMONSEL results and BSE saturation points show similar trends. The large deviation of the experimental ETD-SE result of Al_2O_3 is considered due to its insulating properties.